Contributions to Plasma Physics

ORIGINAL ARTICLE OPEN ACCESS

Thermal Conduction in Laser-Driven Tin Plasmas and the Sensitivity of Plasma Properties to the Flux Limiter

S. Aggarwal[1,2] | J. Gonzalez[1,2,3] | S. J. J. de Lange[1,2] | J. Sheil[1,2]

[1]Advanced Research Center for Nanolithography, Amsterdam, the Netherlands | [2]Department of Physics and Astronomy, and LaserLaB, Vrije Universiteit, Amsterdam, the Netherlands | [3]Department of Applied Physics, Escuela Técnica Superior de Ingeniería Aeronáutica y del Espacio, Universidad Politécnica de Madrid, Madrid, Spain

Correspondence: S. Aggarwal (s.aggarwal@arcnl.nl) | J. Sheil (j.sheil@arcnl.nl)

Received: 2 March 2026 | **Revised:** 17 July 2026 | **Accepted:** 5 August 2026

ABSTRACT

We study the role of thermal conduction in laser-produced tin plasma sources of extreme ultraviolet (EUV) light using radiation-hydrodynamic simulations. Adopting the flux-limited Spitzer–Härm approach, we investigate the sensitivity of the electron temperature, electron density, net in-band emissivity, and conversion efficiency to the choice of flux limiter for plasmas driven by two laser wavelengths: $\lambda_{laser} = 10.6$ and 2 µm. For plasmas driven by $\lambda_{laser} = 10.6$ µm laser light, the plasma properties are highly sensitive to flux limiters in the range $0.01 \leq f \leq 0.2$, which originates from the choice of heat flux (either Spitzer–Härm or free-streaming) adopted in the simulations. The conversion efficiency is found to increase sharply from 2% to 5% with increasing f in this range owing to the increased population of EUV-emitting charge states in the plasma. By quantifying the Knudsen number, we find that SH theory is not valid in the underdense corona in these plasmas. Plasmas driven by 2 µm-wavelength lasers are, on the contrary, largely insensitive to the choice of f given the higher electron densities and dominance of the free-streaming heat flux. We find that Spitzer–Härm theory is valid in these plasmas.

1 | Introduction

An accurate description of energy-transport processes in laser-produced plasmas (LPPs) is essential for predicting and understanding the outcomes of experiments [1–6]. Thermal conduction is one such process, whose theory was put on a firm foundation in the work of Spitzer and Härm [7] more than 70 years ago. Core to Spitzer–Härm (SH) theory is the treatment of distant encounters in the plasma using a diffusion term in the Boltzmann equation [8], which leads to the well-known expression for the heat flux $\mathbf{Q}_{SH} = -\kappa_{SH}\nabla T_e$ where κ_{SH} is the SH thermal conduction coefficient and T_e is the electron temperature [9]. The theory is built on the assumption that the length scale of electron temperature variations $L_T = T_e/|\nabla T_e|$ is much larger than the electron mean-free-path $\lambda_e = T_e^2/\left(4\pi n_e z_{ion} e^4 \ln\Lambda\right)$, where e is the elementary charge, n_e is the free-electron density, z_{ion} is the average charge state of the plasma and $\ln\Lambda$ is the Coulomb logarithm [10]. The Knudsen number $K_n \equiv \lambda_e/L_T$ is thus a measure of the validity of the theory; values as low as $K_n \lesssim 0.01$ are required given the long mean free paths of high-velocity electrons that govern heat transport [1, 11].

In situations where the Knudsen number is larger or closer to 0.01, for example, in steep temperature gradients encountered in direct- [12] and indirect-driven [13] fusion plasmas, heat transport is no longer a local, diffusive process. High-velocity electrons, with their long mean free paths, easily stream down the temperature gradient and deposit their energy in a region often far removed from where ∇T_e is large; this is known as non-local heat transport. It has been consistently shown [14, 15] that SH theory *underestimates* the heat flux in this "downstream" region and *overestimates* the heat flux where ∇T_e is large. A proper description of non-local heat transport requires a kinetic approach where the electron distribution function is obtained by numerically solving the Vlasov-Fokker-Planck (VFP) equation [11, 14, 16]. Solving this equation in two or three-dimensions is, however, very computationally expensive, especially if one wants to incorporate laser absorption or atomic kinetic processes in the model [17]. To circumvent these challenges, reduced non-local transport models were developed for use in hydrocodes, such as the convolution kernel approaches of Luciani-Mora-Virmont (LMV) [15], Schurtz-Nicolai-Busquet (SNB) [18], and Manheimer-Colombant-Goncharov (MCG) [19]. Recent years have witnessed significant activity in benchmarking these models against VFP simulations [13, 20–24]. That said, their implementation in large-scale radiation-hydrodynamic (RH) codes still leads to unfavorably long computation times [24].

As a result, RH codes very often implement SH theory together with a correction procedure. One approach is to use a *dynamic* heat flux Q that takes the smaller of two values: the SH heat flux $|\mathbf{Q}_{SH}| \equiv Q_{SH}$ or the flux-limited free-streaming flux [12, 25–27],

$$fQ_{FS} = fn_e T_e \sqrt{T_e/m_e}. \tag{1}$$

This condition is typically written $Q = \min(Q_{SH}, fQ_{FS})$. The free streaming flux Q_{FS} represents an upper bound to the heat flux, derived in the assumption that the energy density ($\propto n_e T_e$) flows at the thermal velocity $v_{th} = \sqrt{T_e/m_e}$. It is typically much larger than the heat flux obtained from kinetic simulations, a difference that is reconciled in hydrocodes by multiplying Q_{FS} by a factor f known as the flux limiter. Appropriate values for f are typically inferred from comparisons with kinetic simulations or experimental measurements [12, 25]. The high-flux model adopted in inertial confinement fusion simulations uses $f = 0.15$, for instance [23, 24, 28] (time dependent flux limiters have also been considered [29–31]).

The goal of the present work is to elucidate the role of thermal conduction in an industrial application of laser-driven plasmas: extreme ultraviolet (EUV) light sources for semiconductor device manufacturing [32–34]. These plasmas are generated by firing CO_2 lasers (laser wavelength $\lambda_{laser} = 10.6\,\mu\text{m}$) onto tin targets. While the plasma radiates across all wavelengths, the most intense emission is concentrated in a narrow wavelength band centered at 13.5 nm [34, 35], which coincides with the reflective wavelengths (the 13.5 ± 0.135 nm "in-band" region) of molybdenum/silicon multilayer mirrors [36]. Atomic transitions from multiply excited states in Sn^{11+}–Sn^{14+} ions are the source of this EUV radiation [37–40]. These ions are bred at electron densities near the critical electron density [27] for CO_2 laser light $n_c \approx 10^{21}\lambda_{laser}^{-2}$ cm^{-3} $\approx 10^{19}$ cm^{-3} and at temperatures $T_e \approx 30$–50 eV [41, 42]. While CO_2 lasers form the backbone of industrial EUV sources, there is growing interest in the use of solid-state Tm:YLF laser systems [43] ($\lambda_{laser} = 2\,\mu\text{m}$) to drive the plasma. Not only do these laser systems exhibit high electrical efficiencies and favorable pulse-shaping capabilities, the tin plasmas they generate can produce high EUV energies and conversion efficiencies (CEs—the ratio of in-band energy radiated in the laser-illuminated half-sphere to the laser energy) [44–50]. Given the inverse square dependence of n_c on λ_{laser}, 2 μm wavelength laser light can propagate to much higher electron densities than 10.6 μm laser light. As a result, the EUV-emitting charge states are bred at densities approximately an order of magnitude higher in the 2 μm case than the 10.6 μm one.

Unlike the field of laser fusion, however, very little attention has been paid to the role of thermal conduction in EUV source plasmas. Studies invoking RH codes have either assumed a fixed value for the flux limiter $f = 0.1$ (such as in works using the codes Star-1D [51], Star-2D [52], RALEF-2D [53, 54], and RHDLPP [55]) or have implemented solely SH theory [56, 57]. The goal of the present work is to build a clearer picture of thermal conduction in EUV source plasmas. We provide answers to the following questions:

1. Is SH theory a valid assumption in $\lambda_{laser} = 10.6$ and 2 μm-driven EUV source plasmas?
2. How do plasma properties (e.g., electron temperature and electron density) depend on the choice of flux limiter?
3. Is the conversion efficiency (CE) sensitive to the choice of flux limiter?

The paper is structured as follows. In Section 2 we describe the thermal conduction model implemented in our RALEF-2D simulations as well as the simulation parameters that were adopted. An analysis of the simulation results is presented in Section 3, where we focus on clarifying the sensitivity of the plasma properties and CE to the flux limiter. An outlook is presented in Section 4, where we discuss experimental and theoretical studies that could benchmark our simulation results, as well as potential modifications to thermal conduction brought about by the Langdon effect [58, 59]. Finally, we conclude the work in Section 5.

2 | Thermal Conduction and Its Implementation in RALEF-2D

We have performed simulations of laser-produced tin plasmas using the RALEF-2D radiation-hydrodynamics code [60]. The code solves the equations of single-fluid, single-temperature hydrodynamics accounting for the processes of laser energy deposition, thermal conduction, and radiation transport. It has found extensive application in modeling EUV source plasmas, from quantifying laser-induced droplet propulsion [61, 62], to predicting ion kinetic energy distributions [63, 64], to characterizing the radiative properties of EUV sources [41, 46, 53, 65]. The code does not implement the Langdon effect [58, 59], the phenomenon where inverse bremsstrahlung absorption drives free electrons into non-Maxwellian distributions (we discuss in Section 4 what this may mean for the results presented in this work).

2.1 | Thermal Conduction in RALEF-2D

We first recall the expression for the heat flux in SH theory:

$$\mathbf{Q}_{SH} = -\kappa_{SH} \nabla T_e. \tag{2}$$

The thermal conduction coefficient κ_{SH} is given by

$$\kappa_{SH} = 20\left(\frac{2}{\pi}\right)^{3/2} \frac{T_e^{5/2}}{\sqrt{m_e} e^4 z_{ion} \ln \Lambda} \epsilon\delta_e, \tag{3}$$

Here z_{ion} is the average charge state defined as $z_{ion} = n_e/n_i$ where n_i is the ion density. The quantities ϵ and δ_e are correction factors that account for induced electric fields and electron–electron scattering, respectively [66]. They are given by

$$\epsilon\delta_e = \frac{15\pi}{256} \frac{45\zeta + 433\zeta^2}{9 + 151\zeta + 217\zeta^2}, \quad \zeta = \frac{1}{4\sqrt{2}} \frac{z_{ion} \ln \Lambda_{ei}}{\ln \Lambda_{ee}}. \tag{4}$$

Here, $\ln \Lambda_{ei}$ and $\ln \Lambda_{ee}$ are the electron-ion and electron–electron Coulomb logarithms, respectively. In a single-fluid framework, $T_i = T_e$ and we can write $\ln \Lambda_{ei} \approx \ln \Lambda_{ee}$. This leads to the following expression for the thermal conduction coefficient:

$$\kappa_{SH} = \frac{375}{128\sqrt{\pi}} \frac{1 + \frac{433}{180\sqrt{2}} z_{ion}}{1 + \frac{151}{36\sqrt{2}} z_{ion} + \frac{217}{288} z_{ion}^2} \frac{T_e^{5/2}}{\sqrt{m_e} e^4 \ln \Lambda}. \tag{5}$$

In plasmas with high electron densities and low temperatures, this expression should be modified to account for the effects of electron degeneracy and electron-atom scattering.

The modified expression implemented in the RALEF-2D code is written [67]

$$\kappa_e = \frac{375}{128\sqrt{\pi}} \frac{\tilde{z}_i + \frac{433}{180\sqrt{2}} \tilde{z}_i^2}{1 + \frac{151}{36\sqrt{2}} \tilde{z}_i + \frac{217}{288} \tilde{z}_i^2} \times \frac{z_{ion} T_e \tilde{T}_F^{3/2}}{\sqrt{m_e} e^4 \left[z_{ion} \tilde{z}_i \ln \tilde{\Lambda} + K_{ea} \tilde{T}_F^{3/2} T_F^{1/2} \max(0, 1 - z_{ion}) \right]}, \tag{6}$$

where

$$\tilde{z}_i = \max(1, z_{ion}) = \begin{cases} z_{ion}, & z_{ion} \geq 1, \\ 1, & z_{ion} < 1. \end{cases} \tag{7}$$

The corrections introduced in Equation (6) are relevant in regions close to the target surface. The term $\max(0, 1 - z_{ion})$ in the denominator of Equation (6) "activates" the contribution of electron-atom collisions to thermal conduction. These collisions are less efficient at transferring heat than electron-ion collisions, and thus the thermal conduction coefficient is reduced when electron-atom collisions are present. The quantity $K_{ea} = \sigma_{ea}/e^4$, where we take a fixed value for the electron-atom scattering cross-section $\sigma_{ea} = 10^{-15}$ cm^{-2}. The Fermi temperature T_F introduced in Equation (6) is given by

$$T_F = \sqrt{T_e^2 + \left(\frac{2}{3} E_F\right)^2}, \tag{8}$$

where $E_F = \frac{\hbar^2}{2m_e} (3\pi^2 n_e)^{2/3}$ is the Fermi energy. In a degenerate plasma (one in which electrons are described by Fermi-Dirac statistics instead of Maxwell-Boltzmann statistics), plasma transport is governed by electrons at the Fermi surface. The quantity $\tilde{T}_F = \sqrt{T_e^2 + (\beta_{ec} E_F)^2}$ where $\beta_{ec} = 0.34$ is a parameter that yields the correct value of κ_e in the limit of $T_e \ll E_F$ for a degenerate Lorentzian plasma [66–68].

As will be discussed in detail in Section 3.1, the most important correction in our work is the Coulomb logarithm $\ln \tilde{\Lambda}$ for electron-ion collisions. The RALEF-2D code implements an interpolation expression proposed in Reference [69] of the form

$$\ln \tilde{\Lambda} = \ln \left[1 + \frac{\Lambda(g_{ec} + \Lambda)}{1 + \Lambda + (6.5 g_{ec} \Lambda)^{-1}} \right], \tag{9}$$

where choosing $g_{ec} = 4.5$ recovers the experimental value of the thermal conduction coefficient of liquid tin [67]. The argument of the Coulomb logarithm, Λ, is given by (page 19 of [67], equation 4.77)

$$\Lambda \approx 3.4 \frac{T_e}{e^2} \left[\lambda_D^{-2} \left(z_{ion}^2 + 0.95 \hbar^2 T_e / m_e e^4 \right) \right]^{-1/2}, \tag{10}$$

where $\hbar$ is the reduced Planck's constant and the Debye length $\lambda_D = \left[4\pi n_e e^2 \left(\frac{1 + z_{ion}}{T_e} \right) \right]^{-1/2}$. When degeneracy effects are taken into account, the FS flux is modified [67] according to,

$$Q_{FS} = n_e T_e \left(\frac{T_F}{m_e} \right)^{1/2}. \tag{11}$$

The RALEF-2D simulations in this work use κ_e for the thermal conduction coefficient, and a comparison with κ_{SH} is presented in Section 3.1 below.

2.2 | RALEF-2D Simulation Parameters

We simulate laser irradiation of 40 µm diameter tin droplets with spatially constant laser profiles of 85 µm in width. The temporal profiles are box-shaped with a rise time of 2 ns and have a sharp cut-off at 27 ns as shown by the red curve in Figure 1. The other quantities shown in Figure 1 are the reflected power P_{ref} (green),

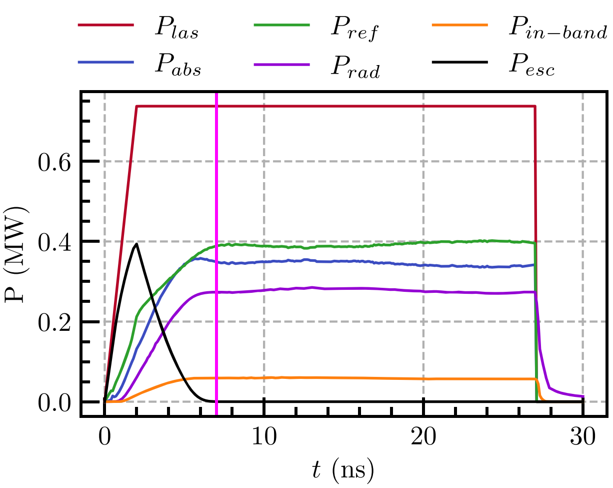

FIGURE 1 | Temporal variation of input laser power P_{las} (red), reflected power P_{ref} (green), in-band power $P_{in-band}$ (orange), absorbed power P_{abs} (blue), radiated power P_{rad} (violet), and escaped power P_{esc} (black), for $\lambda_{laser} = 10.6$ µm and $I_{laser} = 1.3 \times 10^{10}$ W cm^{-2}. The magenta line marks the time $t = 7$ ns at which the analysis is performed.

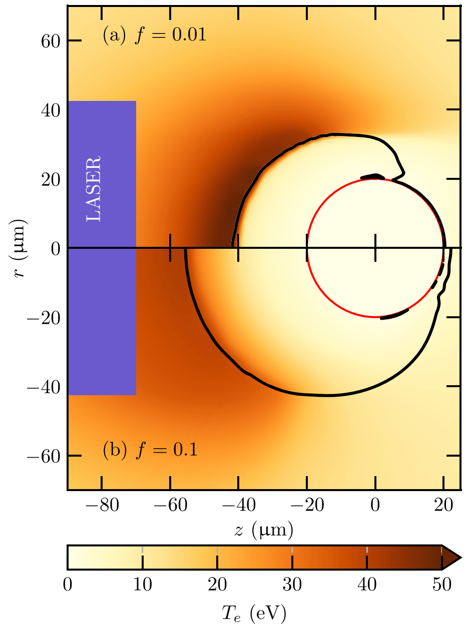

FIGURE 2 | Spatial distribution of electron temperature for flux limiter values (a) $f = 0.01$ and (b) $f = 0.1$ for $\lambda_{laser} = 10.6\,\mu m$ and $I_{laser} = 1.3 \times 10^{10}$ W cm^{-2}. The images represent a snapshot of the plasma 7 ns after the laser is turned on. The black contour is the critical electron density surface ($n_c \approx 10^{19}$ cm^{-3}) and the red circle depicts the boundary of the droplet at $t = 0$ ns. The 85 μm width of the laser profile is indicated by the purple box.

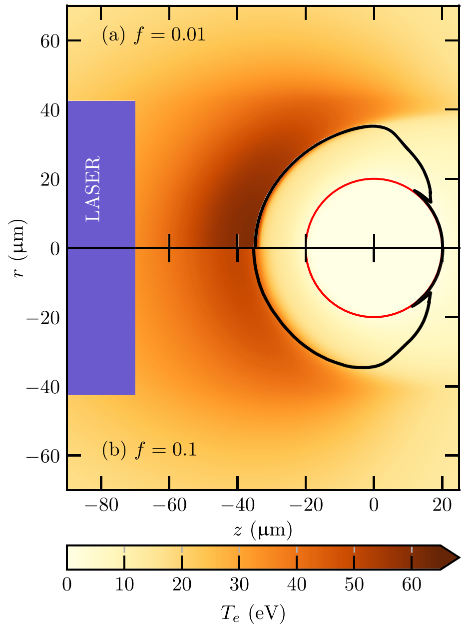

FIGURE 3 | Same as Figure 2 for $\lambda_{laser} = 2\,\mu m$ irradiation for $I_{laser} = 7 \times 10^{10}$ W cm^{-2} and $n_c \approx 2.8 \times 10^{20}$ cm^{-3}.

in-band power $P_{in-band}$ (orange), absorbed power P_{abs} (blue), radiated power P_{rad} (violet), and escaped power $P_{esc} = P_{las} - (P_{abs} + P_{ref})$ (black). Two laser wavelengths $\lambda_{laser} = 10.6$ and 2 μm are considered, each having an intensity of $I_{laser} = 1.3 \times 10^{10}$ and 7×10^{10} W cm^{-2} respectively. This choice is based on an experimentally motivated scaling [53] of the optimal CE with laser intensity of the form $I_{laser} = (1.4 \times 10^{11})/\lambda_{laser}$ W cm^{-2}.

Following the initial plasma formation phase, the reflected laser power, the absorbed laser power, and in-band emission are constant in time, indicating that the plasma has entered a quasi-steady-state regime [53, 65] at $t \sim 7$ ns. The time it takes the plasma to reach a quasi-steady-state depends on the hydrodynamic timescale $t_h \sim R/c_s$ [65] where R is the characteristic radius of the sonic surface and c_s is the sound speed in the corona. For CO_2-driven plasmas, the sonic surface lies closer to the critical surface [65]. At $R \approx 40$ μm, $T_e \approx 20$ eV and $z_{ion} \approx 6$ (parameters in the vicinity of the critical surface for the $f = 0.01$ case shown in Figure 2), $t_h \approx 4$ ns. This value is commensurate with the time $t \approx 7$ ns for the plasma to reach a quasi-steady-state regime. In Figure 2 we present two-dimensional profiles of electron temperature for $\lambda_{laser} = 10.6\,\mu m$ irradiation of tin droplets for simulations that use a flux limiter of (a) $f = 0.01$ and (b) $f = 0.1$. The $\lambda_{laser} = 2\,\mu m$ cases are shown in Figure 3. The images represent "snapshots" of the plasma 7 ns (shown by the magenta line in Figure 1) after the laser is turned on (steady-state conditions are established by this time). The laser propagates from left to right, and the purple box indicates the 85 μm width of the flat-top laser profile. The red circle indicates the boundary of the droplet at $t = 0$ ns, and the black contour represents the position of the critical electron density surface $n_c \approx 10^{21}\,\lambda_{laser}^{-2}$ cm^{-3}. Comparing panels (a) and (b) in both cases, we see that smaller values of f yield higher electron temperatures, especially near the critical electron density surface. The electron density profile in the $\lambda_{laser} = 10.6\,\mu m$ case is also strongly modified, as evidenced by the shape of the critical electron density surface. As will soon become clear, this behavior originates from different values for the heat fluxes that are adopted in the simulations. In the remainder of this publication, we will present our results in the form of one-dimensional spatial profiles of plasma quantities taken along the z axis; they will be referred to as "lineouts." This will enable a clearer, more quantitative comparison of plasma parameters and gradients that are difficult to discern from two-dimensional color maps.

3 | Results

Before proceeding with a detailed analysis of the simulation results, we first compare the thermal conduction coefficient implemented in the RALEF-2D simulations, κ_e, with the SH one κ_{SH}.

3.1 | Corrections to the Thermal Conduction Coefficient

In Figure 4a we plot a lineout of the ratio κ_{SH}/κ_e (red curve) for $\lambda_{laser} = 10.6\,\mu m$ irradiation and $f = 0.01$. In the high-temperature region ($z < -42\,\mu m$), $\kappa_{SH}/\kappa_e \simeq 1$ as expected. With increasing z, n_e increases (see Figure 5d below), T_e and z_{ion} decrease, and κ_{SH}/κ_e increases. Neither T_F nor $\tilde{T}_F$ is responsible for this increase; they both lie atop the T_e curve as seen in Figure 4a. The close agreement between the temperatures occurs because the corrections are insignificant in this region. The Fermi energy E_F for the electron densities in this region are of the order $E_F \sim 0.02 - 0.14$ eV, much smaller than the electron temperature

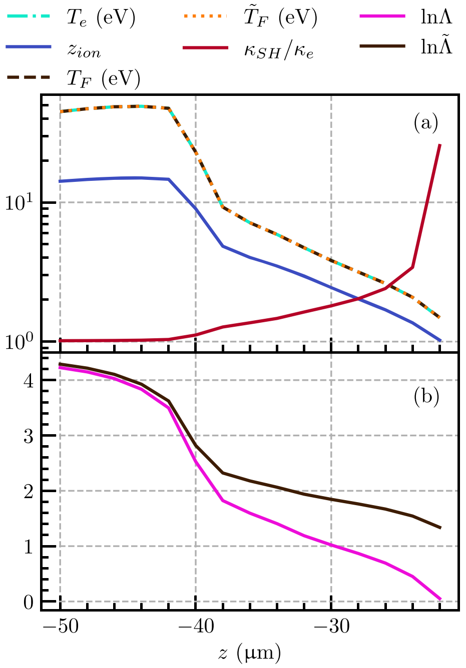

FIGURE 4 | Spatial variation of (a) the ratio κ_{SH}/κ_e (red; solid), T_e (cyan; dashed-dotted), T_F (black; dashed), $\tilde{T}_F$ (orange; dotted), z_{ion} (blue; solid) and (b) $\ln\Lambda$ (pink; solid) and $\ln\tilde{\Lambda}$ (black; solid) for $\lambda_{laser} = 10.6$ μm irradiation and $f = 0.05$.

$T_e \sim 10 - 40$ eV. Consequently, from Equation (8), $T_F \approx T_e$. The same reasoning applies to $\tilde{T}_F$. The three temperatures only begin to diverge in the dense, cooler region near the droplet surface (not shown in Figure 4), where the corrections included in Equation (6) become relevant. Therefore, the temperatures T_F and $\tilde{T}_F$ can be ruled out as the cause of the increase in κ_{SH}/κ_e. It is actually the modified Coulomb logarithm $\ln\tilde{\Lambda}$ that is the culprit. In Figure 4b, we plot this quantity alongside $\ln\Lambda$, where it is evident that they start to depart from each other at exactly the point where κ_{SH}/κ_e increases. In fact, if $T_e = T_F = \tilde{T}_F$ and $z_{ion} > 1$, then $\kappa_{SH}/\kappa_e = \ln\tilde{\Lambda}/\ln\Lambda$. This explains the increase of κ_{SH}/κ_e with increasing z.

3.2 | The Role of the Flux Limiter

We now investigate the sensitivity of the heat flux $Q = \min(Q_{SH}, fQ_{FS})$, the plasma properties, and the CE to the choice of flux limiter f.

3.2.1 | 10.6 μm-Driven Plasmas

In Figure 5a we plot the magnitude of the heat flux Q for $f = 0.05$ (red), $f = 0.1$ (blue) and $f = 0.3$ (green). Since the chosen heat flux is $Q = \min(Q_{SH}, fQ_{FS})$, two distinct line styles are used to highlight the regions where the heat flux is governed by $Q = Q_{SH}$ (Equation 2, solid lines) and where it is governed by $Q = fQ_{FS}$ (Equation 11, dashed lines). For $f = 0.3$, the heat flux is $Q = Q_{SH}$ everywhere for $z > -115$ μm. For $f = 0.05$ and $f = 0.1$, we see that $Q = Q_{SH}$ for $z > -45$ μm and $z > -50$ μm, respectively, and also where sharp dips appear in the profile. These sharp dips are present where T_e (see Figure 5b) reaches its global maximum and

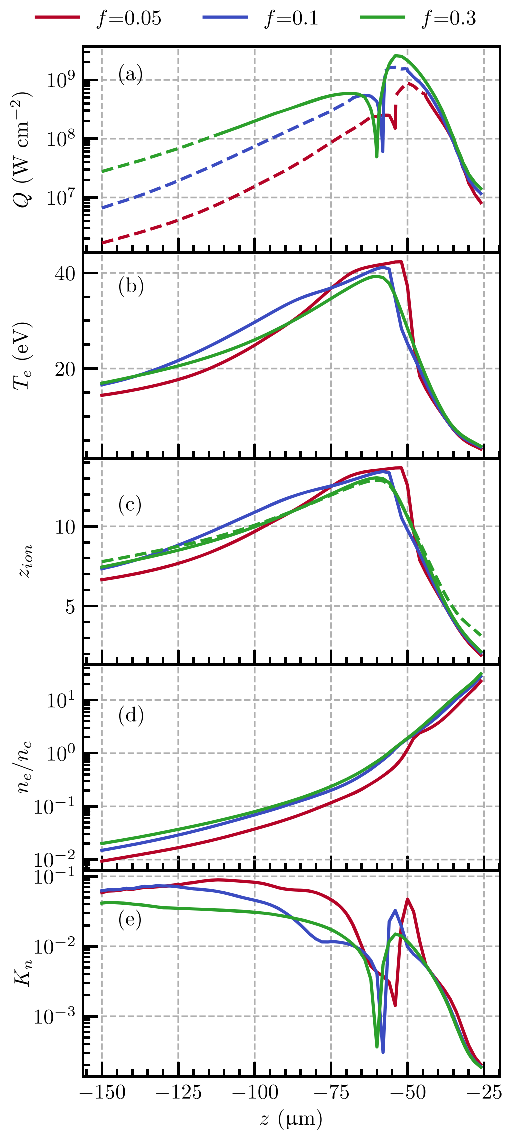

FIGURE 5 | Lineouts of various quantities taken along the z-axis: (a) the heat fluxes Q_{SH} (solid lines) and fQ_{FS} (dashed lines), (b) electron temperature T_e, (c) average charge state z_{ion}, (d) electron density normalized by the critical electron density n_e/n_c, and (e) Knudsen number K_n for $f = 0.05$ (red), 0.1 (blue), and 0.3 (green) for $\lambda_{laser} = 10.6$ μm irradiation with $I_{laser} = 1.3 \times 10^{10}$ W cm^{-2}. The dashed line in plot (c) represents the average charge state z_{ion} evaluated using the power-law relation $z_{ion} = 22.5\, T^{0.6}$ [65].

thus ∇T_e and Q_{SH} attain small values. Perhaps the most important takeaway from this plot is that for $z < -75$ μm, the heat flux for the $f = 0.05$ and $f = 0.1$ cases are significantly smaller than the $f = 0.3$ case. This is important for the analysis of the plasma properties below.

In Figure 5b,d we present lineouts of the electron temperature T_e and critical density-normalized electron density profiles n_e/n_c, respectively. The temperature profiles peak where the laser deposits most of its energy: just in front of the critical electron density $n_c \approx 10^{19}$ cm^{-3} (which corresponds to $n_e/n_c = 1$ in Figure 5d). Presented in Figure 5c are lineouts of the average charge state z_{ion} for the three flux limiter cases. The dashed line represents the power-law relation $z_{ion} = 22.5\ T^{0.6}$ [65] for the $f = 0.3$ case, which aligns very well with the RALEF-2D data. For $z < -70\ \mu m$, the temperature profile and z_{ion} in the $f = 0.05$ case decreases more rapidly with decreasing z than the $f = 0.1$ and $f = 0.3$ cases. For regions where $n_e/n_c > 1$, the temperature profile in the $f = 0.05$ case exhibits a steeper gradient than in the $f = 0.1$ and 0.3 cases; a similar observation was made in the work of Colombant et al. [70]. For a given $z < -50\ \mu m$, n_e/n_c is smallest in the $f = 0.05$ case. We attribute this to differences in the nature and magnitude of the heat fluxes shown in Figure 5a. The lower heat fluxes in the $f = 0.05$ and 0.1 cases result in lower energy and mass transport into the underdense region compared to the $f = 0.3$ case. In Figure 5e we plot the Knudsen number $K_n = \lambda_e/L_T$. The dips correspond to regions where $\nabla T_e \simeq 0$, as T_e reaches a maximum and thus $L_T = T_e/|\nabla T_e|$ becomes large. For all f values shown in Figure 5, the criterion $K_n \lesssim 0.01$ is violated in the majority of the underdense region. While SH theory is not implemented in the $f = 0.05$ and 0.1 cases (because $Q = fQ_{FS}$), the large temperature gradient may enhance the effects of non-local heat transport that may not be accurately reflected by the free-streaming flux. What is more worrisome is that SH theory is (i) implemented and (ii) violated in a large part of the underdense corona ($z < -65\ \mu m$) for the $f = 0.3$ case. This casts doubt on the reliability of the heat flux model employed in these simulations. This reinforces the need for non-local modeling of thermal conduction in these plasmas.

3.2.2 | 2 μm-Driven Plasmas

We now turn our attention to the $\lambda_{laser} = 2\ \mu m$ case. In Figure 6 we present lineouts of the same quantities as that shown in Figure 5 for $f = 0.01$ (red), $f = 0.05$ (blue), and $f = 0.1$ (green). The much higher densities in the $\lambda_{laser} = 2\ \mu m$ case lead to much higher free-streaming fluxes $Q_{FS} \propto n_e T_e^{3/2}$ compared to the $\lambda_{laser} = 10.6\ \mu m$ case (the higher temperatures near the critical surface further amplify Q_{FS} in this region). This means that very small values of f are needed for $Q = \min(Q_{SH}, fQ_{FS}) = Q_{SH}$. Similar to the $\lambda_{laser} = 10.6\ \mu m$ case, the peak temperature in the lower flux limiter case ($f = 0.01$) is higher than the larger flux limiter cases ($f = 0.05$ and 0.1), and the densities in the corona are approximately a factor two higher in the latter. Unlike the $\lambda_{laser} = 10.6\ \mu m$ case, however, the temperature profile in the $f = 0.1$ case (where $Q = Q_{SH}$) is much steeper for densities larger than n_c.

Increasing f beyond 0.01, as shown in Figure 6 for $f = 0.05$ and $f = 0.1$, essentially pushes fQ_{FS} closer to Q_{SH}. The T_e, n_e/n_c, and K_n profiles are very similar among the $f = 0.05$ and 0.1 cases. Importantly, all cases (including $f = 0.01$) exhibit $K_n \lesssim 0.01$, meaning that SH theory is valid in all cases. This places confidence in the thermal conduction modeling we conducted in our previous works [46, 53].

3.2.3 | Impact of Flux Limiter on Thermal Conduction and Net Radiated Power

Having established how the flux limiter alters the plasma profiles, we now examine how it influences the thermal conduction and radiative properties of the plasma. To do this, we compare the 1D profiles (taken along the z-axis) of the net radiated power ζ_{rad} and the quantity $-\partial Q/\partial z$ normalized to the laser input power. $-\partial Q/\partial z$ determines whether a given region of plasma receives or transfers energy through conduction, which motivates comparing it directly against the net radiated power. ζ_{rad} is the net radiated power per unit volume, integrated over the entire emission and absorption spectrum. A positive value of ζ_{rad} indicates emission; and negative value indicates absorption.

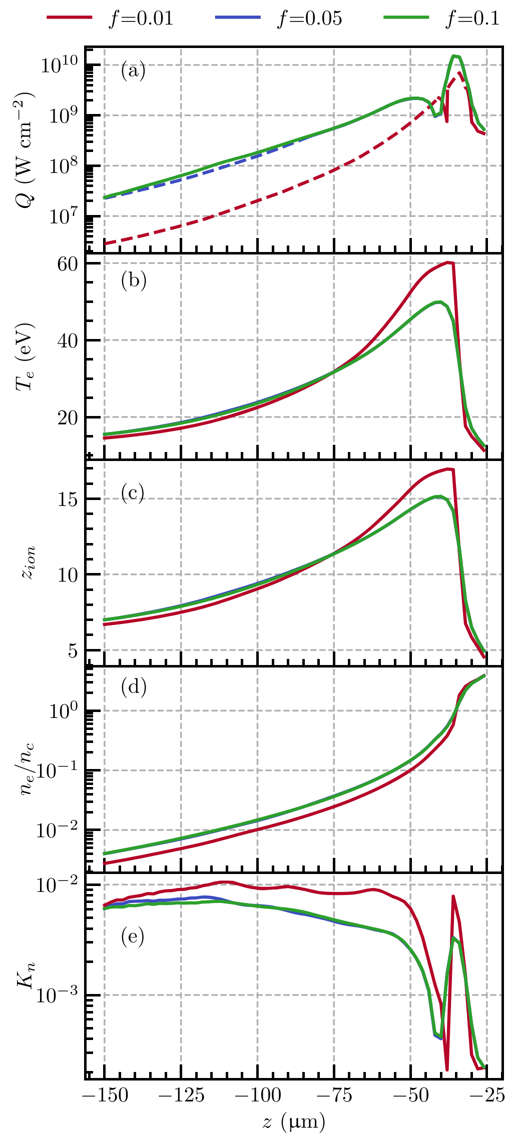

FIGURE 6 | Same as Figure 5 for $\lambda_{laser} = 2\ \mu m$ irradiation with $I_{laser} = 7 \times 10^{10}\ W\ cm^{-2}$ where $f = 0.01$ (red), 0.05 (blue), and 0.1 (green). The solid line in (a) corresponds to Q_{SH} and the dashed line corresponds to fQ_{FS}.

In Figure 7 we present the comparison of ζ_{rad} with $-\partial Q/\partial z$, for $f = 0.05$ and 0.1 for $\lambda_{laser} = 10.6\ \mu m$. The dotted vertical lines represent the critical electron density surface position in each case. The dashed lines show $-\partial Q/\partial z$; $-\partial Q/\partial z$ is negative wherever the rate at which the temperature gradient change in space is negative, i.e., $\partial^2 T/\partial z^2 < 0$ (e.g., close to the peak temperature) and is positive wherever $\partial^2 T/\partial z^2 > 0$.

Increasing the flux limiter from $f = 0.05$ to 0.1 results in a noticeable broadening of the ζ_{rad} profile, which we attribute to the

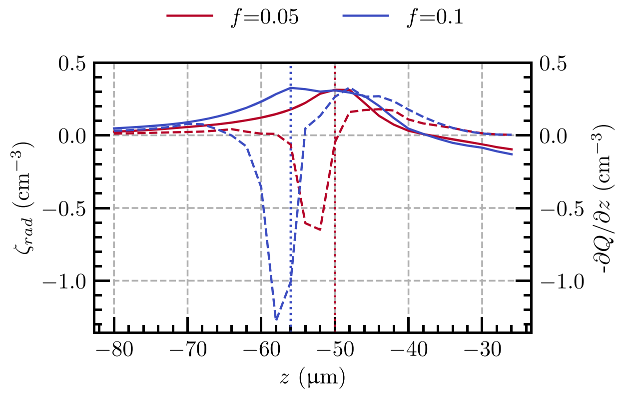

FIGURE 7 | Spatial variation of net radiated power ζ_{rad} (solid lines) and the quantity $-\partial Q/\partial z$ (dashed lines) normalized to laser input power for flux limiter values $f = 0.05$ (in red) and $f = 0.1$ (in blue) for $\lambda_{laser} = 10.6\,\mu m$ and $I_{laser} = 1.3 \times 10^{10}$ W cm^{-2}. The dotted vertical lines represent the positions of the critical electron density in each case.

increase in plasma density at ever-larger distances from the target surface (see Figure 5d). The effect on $-\partial Q/\partial z$ is a shifting of the profile to a narrower axial region and a corresponding enhancement of the maximum values.

Closer to the critical surface ($-60\ \mu m \le z \le -50\ \mu m$), $-\partial Q/\partial z$ develops a sharp, localized negative feature, indicating a narrow region of strong conductive cooling. This coincides with the location where T_e reaches its global maximum (see Figure 5b), where $\nabla T_e \approx 0$ and Q_{SH} correspondingly collapses to a local minimum, producing the sharp dip in Q already identified in Section 3.2.1.

Near the peak of net emission ($z \approx -50\ \mu m$), $-\partial Q/\partial z$ rises sharply and becomes comparable in magnitude to ζ_{rad}. This coincides with the transition of Q from the flux-limited free-streaming regime ($Q = fQ_{FS}$) back to $Q = Q_{SH}$ (Section 3.2.1). Beyond the peak, the two quantities remain similar in magnitude, as both the conduction and radiation depend on the same decrease in T_e and z_{ion} towards the cooler and denser plasma near the droplet.

These results show that conduction and radiation do not contribute equally throughout the plasma. Radiation dominates the underdense corona, while conduction becomes locally important wherever Q develops sharp features: near the temperature peak and near the Q_{SH}/fQ_{FS} transition, close to the critical surface. We further discuss the influence of the flux limiter on the radiative properties of the plasma in the following section.

3.2.4 | Impact of Flux Limiter on the Net In-Band Emission, Optical Depth and Conversion Efficiency

In this section, we first quantify how the flux limiter influences the net in-band emissivity. Figures 8 and 9 show the net in-band radiated power per unit volume $\zeta_{in-band}$, normalized by the input laser power, at $t = 7$ ns for different f values and for $\lambda_{laser} = 10.6\,\mu m$ [53]. The solid olive contour represents the critical electron density surface, and the dashed lines represent regions of constant average charge state z_{ion}. Regions of net emission—located near the critical surface—are shown in red, while regions of net absorption appear in blue. Consistent with

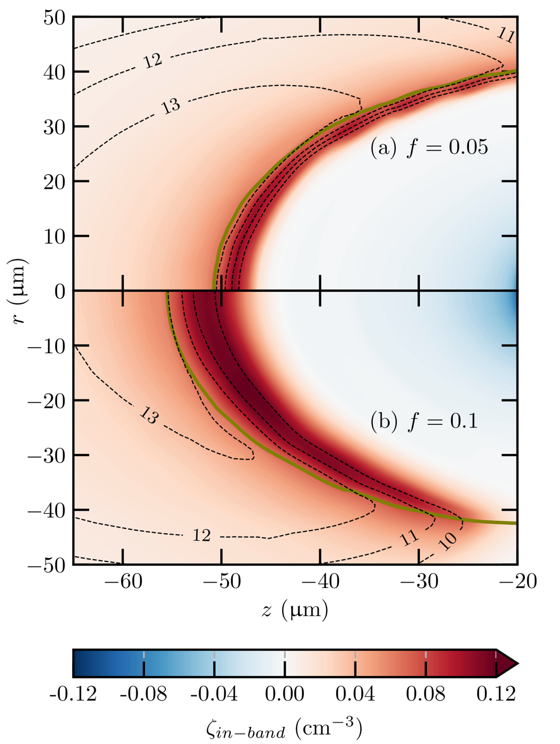

FIGURE 8 | Spatial distribution of in-band power normalized to laser input power $\zeta_{in-band}$ for flux limiter values (a) $f = 0.05$ and (b) $f = 0.1$ for $\lambda_{laser} = 10.6\,\mu m$ and $I_{laser} = 1.3 \times 10^{10}$ W cm^{-2}. The images represent a snapshot of the plasma 7 ns after the laser is turned on. The dashed black contours show the average charge state z_{ion} with increments of 1. The solid olive contour is the critical electron density surface ($n_c \approx 10^{19}$ cm^{-3}).

the simulation results in Reference [53], the net-emission zone forms behind the critical surface.

Focusing on Figure 8, we see that the region of net in-band emission is narrower in the $f = 0.05$ case than in the $f = 0.1$ case. This can be understood by examining the average charge state of the plasma z_{ion}, variations of which ultimately boil down to variations in T_e and n_e. Recall that the optimal average charge states for in-band emission lie in the range $z_{ion} \in [10, 14]$ [37, 38] and that z_{ion} scales with T_e according to [65, 71] $z_{ion} \propto T_e^{0.6}$. Comparing the $f = 0.05$ and $f = 0.1$ cases in Figure 8, we see that the charge states responsible for optimal EUV emission are bred in a narrower region in the $f = 0.05$ case. This narrowing originates from the steepness of the temperature profiles associated with the smaller flux limiter values (see Section 3.2.1). The regions of optimal z_{ion} are nearly identical in the $f = 0.2$ and 0.5 cases; see Figure 9. This is because the heat flux saturates at the classical SH value $Q = Q_{SH}$ throughout the plasma and the profiles cease to change with increasing f. For $\lambda_{laser} = 2\,\mu m$, only minor differences appear in the net in-band emissivity at small f values due to the different heat fluxes governing the plasma profiles, which give rise to slightly different temperature and density profiles (see Figure 6).

To have a simplified picture of the 2D profiles shown in Figure 8, we present the lineouts of $\zeta_{in-band}$ (dashed lines), in Figure 10. The profiles in Figure 10 are spatially shifted relative to their

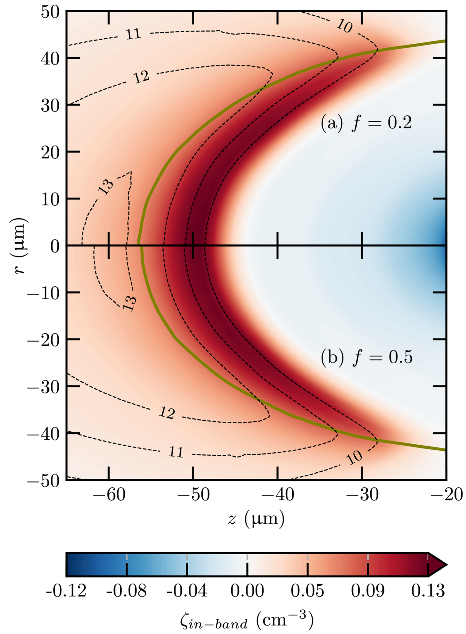

FIGURE 9 | Same as Figure 8 for (a) $f = 0.2$ and (b) $f = 0.5$.

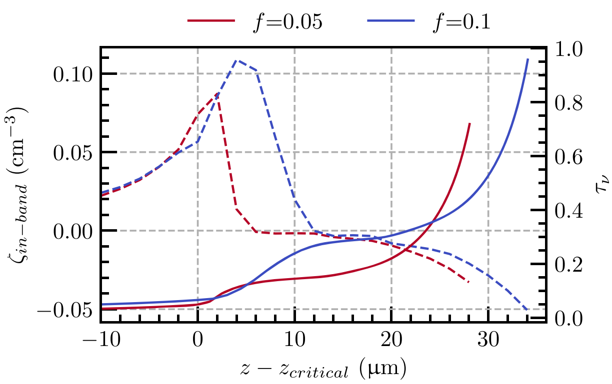

FIGURE 10 | Lineouts of optical depth τ_ν (solid lines) and net in-band power normalized to laser input power $\zeta_{in-band}$ (dashed lines) for flux limiter values $f = 0.05$ (red) and 0.1 (blue) for $\lambda_{laser} = 10.6$ μm and $I_{laser} = 1.3 \times 10^{10}$ W cm^{-2}. The spatial coordinate is shifted by the position of the critical surface $z_{critical}$ such that $z - z_{critical} = 0$ corresponds to the critical electron density surface.

respective critical surfaces $z_{critical}$, such that $z - z_{critical} = 0$ corresponds to the critical surface position. In addition, we have shown the optical depth τ_ν (solid lines) in Figure 10, evaluated in the in-band region. Optical depth τ_ν is the integral of the absorption coefficient $\alpha_\nu(z')$: $\tau_\nu(z) = \int_z^{-\infty} \alpha_\nu(z')\,dz'$ [46]. The optical depths for $f = 0.05$ and $f = 0.1$ are very similar in the region where the two $\zeta_{in-band}$ profiles overlap. However, in the region just behind the critical surface where the $f = 0.1$ case exhibits stronger net emission, the optical depth is larger for $f = 0.1$ than for $f = 0.05$. This is due to enhanced n_e and z_{ion} in this region for the $f = 0.1$ case, consistent with the broader emission zone as seen in Figure 8.

We are now in a position to quantify the sensitivity of the conversion efficiency (CE) of the plasmas to the flux limiter. In-band radiation that intercepts the collector mirror (located in the laser-illuminated half-sphere) is directed into the EUV scanner for use in lithography, and the CE quantifies the efficiency of this process. The results are presented in Figure 11. Here we see that the CE for the $\lambda_{laser} = 10.6$ μm case increases sharply from CE ≈ 2% for $f = 0.01$ to CE ≈ 5% for $f = 0.2$, a significant variation in the context of EUV production. We attribute this behavior to the widening of the net in-band emission region with only a minimal increase in optical depth, as shown in Figures 8–10. The 2 μm case exhibits a near-constant CE ≈ 5% for all f values.

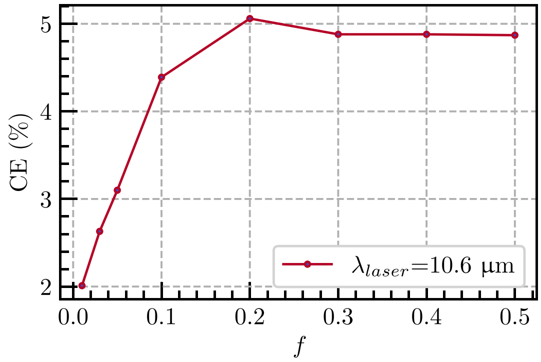

FIGURE 11 | Dependence of CE on f for $\lambda_{laser} = 10.6$ μm.

4 | Outlook

The key learnings to distill from the above discussion are that (i) 2 μm-driven plasma properties are largely insensitive to the choice of f, especially for $f > 0.1$ where $Q = Q_{SH}$ everywhere, and (ii) 10.6 μm-driven plasma properties exhibit a strong sensitivity to f given the lower values of Q_{FS} as a result of the lower plasma densities (as compared to the $\lambda_{laser} = 2$ μm case). This latter finding begs the following question: what is an appropriate value of f for $\lambda_{laser} = 10.6$ μm-driven plasmas? It would be very instructive to compare our results to VFP simulations [21, 22] or RH codes that implement non-local heat transport models [23, 24]. Experimental measurements of the heat flux are the "holy grail" for benchmarking simulations [1, 2], and knowledge of spatially and temporally-resolved temperature and density profiles from Thomson scattering experiments can help eliminate certain f values, such as was done in the recent work of Farmer et al. [23, 24]. Experimental measurements of electron temperatures and densities in laser-driven tin plasmas have been reported in recent years [72–74], albeit for geometries different to those studied in the present work. That said, experimental measurements of this nature can serve as an excellent testing ground for thermal conduction models.

Finally, we wish to comment on the Langdon effect and what our omitting it in the simulations could mean for the results presented in this work. The Langdon effect is the phenomenon where inverse bremsstrahlung absorption distorts the electron distribution function into one that resembles a super-Gaussian function of the form $f_e(v) \propto \exp\left[-\left(v/v_m\right)^m\right]$, where m is the order of the super-Gaussian, $v_m^2 \equiv \frac{3\Gamma(3/m)}{\Gamma(5/m)} v_{th}^2$, and Γ is the gamma function [75]. Compared to an (equilibrium) Maxwellian distribution at the same temperature, a super-Gaussian distribution exhibits fewer low- and high-velocity electrons, and larger numbers of near-thermal electrons. Mora and Yahi [76] and others [77, 78] have shown that this suppression of high-velocity electrons can lead to a significant reduction in thermal conduction. As described by Huo et al. [79], the expression for the heat flux should be modified to account for gradients in n_e and m as follows:

$$Q^* = -\left(C_T \kappa_{SH} \nabla T_e + C_n \kappa_{SH} T_e \frac{\nabla n_e}{n_e} + C_m \kappa_{SH} T_e \frac{\nabla m}{m} \right). \quad (12)$$

We recently quantified the corrections C_T, C_n, and C_m for EUV light source conditions [59]. Considering $\lambda_{laser} = 10.6$ μm-driven conditions near the critical surface (where the laser deposits most of its energy [41]), we have $I_{laser}\lambda_{laser}^2 \sim 10^{12}$ W cm^{-2} μm^2 and $0.2 \lesssim z_{ion}/T_e \lesssim 0.3$, which gives $m \sim 2.3$, $0.75 \lesssim C_T \lesssim 0.8$ and $-0.6 \lesssim C_m \lesssim -0.55$ ($C_n \approx 0$ [59]). With the corrections C_T and C_m being of opposite sign, and our not knowing the magnitude of the $\nabla m/m$ term (it is likely to be small, however), it is difficult to say how large the corrections to the thermal conductivity will be. Neglecting for a moment the $\nabla m/m$ term, the correction C_T will bring Q^* closer to fQ_{FS}, which means that fluctuations in plasma parameters may be seen for an even wider range of f values. It should be mentioned that Shaffer et al. [78] have recently proposed a compact model, supported by VFP simulations, to evaluate corrections to κ_{SH} when non-Maxwellian distributions are present in the plasma. For $\lambda_{laser} = 2$ μm-driven plasmas, $m \sim 2$ due to the lower value of $I_{laser}\lambda_{laser}^2$, and thus one would expect corrections due to non-Maxwellian electrons to be smaller than in the $\lambda_{laser} = 10.6$ μm case. A proper evaluation of the effects of non-Maxwellian electrons on thermal conduction in EUV source plasmas will be pursued in future work.

5 | Conclusions

We have investigated thermal conduction in laser-driven tin plasmas using the flux-limited Spitzer-Harm approach. While strictly a "local" approach, the method provides a simple means of limiting the unphysically high heat fluxes encountered in RH simulations when SH theory breaks down, that is, in the presence of strong temperature gradients. Our primary goal was to quantify the sensitivity of plasma properties, specifically the electron temperature, density, and CE to changes in the flux limiter for $\lambda_{laser} = 10.6$ and 2 μm-driven tin plasmas. Plasma properties for the $\lambda_{laser} = 10.6$ μm-driven case exhibited a strong sensitivity to simulations that use $f \leq 0.2$. Increasing f beyond $f = 0.01$, we found that (i) the temperature profiles became less steep near the critical electron density, (ii) the electron density in the underdense corona increased, and (iii) the CE increased sharply. We attribute this behavior to differences in the SH and free-streaming heat fluxes, the smaller of the two being implemented in the simulations. A complementary analysis of the net in-band emission and in-band optical depth τ_ν reveals that the reduced CE at lower flux limiter values arises from the narrowing of the optimal-charge-state emission zone. Finally, we found that SH theory is violated in large parts of the underdense corona for all f values.

Plasmas driven by $\lambda_{laser} = 2$ μm laser light exhibit much higher electron densities than the $\lambda_{laser} = 10.6$ μm case. As such, the free-streaming flux $Q_{FS} \propto n_e T_e^{3/2}$ is significantly larger than the SH one, meaning that very small values of $f \sim 0.01 - 0.05$ are required for $Q = \min(Q_{SH}, fQ_{FS}) = Q_{SH}$. Plasma properties obtained from simulations with $f = 0.05$ and 0.1 were found to be very similar. The $f = 0.01$ profile exhibited an enhanced temperature near the critical surface and lower electron densities in the corona. The CE was found to be remarkably constant for all flux limiter values, which is due to the similar temperature and density profiles in all cases. We also found that SH theory is valid for all values of f. Finally, we identified experiments that could help identify appropriate values of f for $\lambda_{laser} = 10.6$ μm plasma simulations, and we also briefly discussed the Langdon effect in the context of the current work.

Acknowledgments

We would like to thank M. Reitsma for useful comments on the paper. This publication is part of the project ARIES with file number 20152 of the research programme VENI, which is (partly) financed by the Dutch Research Council (NWO) under an NWO grant. This work was conducted at the Advanced Research Center for Nanolithography, a public–private partnership between the University of Amsterdam, Vrije Universiteit Amsterdam, University of Groningen, the Netherlands Organization for Scientific Research (NWO), and the semiconductor equipment manufacturer ASML.

Funding

This work was supported by Nederlandse Organisatie voor Wetenschappelijk Onderzoek (20152) and was (partly) financed by "Toeslag voor Topconsortia voor Kennis en Innovatie (TKI)" from the Dutch Ministry of Economic Affairs.

Conflicts of Interest

The authors declare no conflicts of interest.

Data Availability Statement

The data that support the findings of this study are available from the corresponding author upon reasonable request.

References

1. R. J. Henchen, M. Sherlock, W. Rozmus, et al., "Observation of Nonlocal Heat Flux Using Thomson Scattering," *Physical Review Letters* 121 (2018): 125001.

2. A. L. Milder, J. Zielinski, J. Katz, et al., "Direct Measurement of the Return Current Instability in a Laser-Produced Plasma," *Physical Review Letters* 129 (2022): 115002.

3. H. Chen, D. T. Woods, W. A. Farmer, et al., "Understanding the Deficiency in Inertial Confinement Fusion Hohlraum X-Ray Flux Predictions Using Experiments at the National Ignition Facility," *Physical Review E* 110 (2024): L013201.

4. W. A. Farmer, M. D. Rosen, H. A. Scott, et al., "Toward an Improved Nonlocal Thermodynamic Equilibrium Model for More Predictive Simulations of Ignition Scale Hohlraums," *Physics of Plasmas* 32 (2025): 072709.

5. D. Turnbull, J. Katz, M. Sherlock, et al., "Inverse Bremsstrahlung Absorption," *Physical Review Letters* 130 (2023): 145103.

6. D. Turnbull, J. Katz, M. Sherlock, et al., "Reconciling Calculations and Measurements of Inverse Bremsstrahlung Absorption," *Physics of Plasmas* 31 (2024): 063304.

7. L. Spitzer and R. Härm, "Transport Phenomena in a Completely Ionized Gas," *Physics Review* 89 (1953): 977–981.

8. R. S. Cohen, L. Spitzer, and P. M. Routly, "The Electrical Conductivity of an Ionized Gas," *Physics Review* 80 (1950): 230–238.

9. We Omit the Boltzmann Constant k_B in Formulae Presented in this Work.

10. The Formulae in This Paper Are Given in Cgs Units.

11. A. R. Bell and M. Sherlock, "The Fast VFP Code for Solution of the Vlasov–Fokker–Planck Equation," *Plasma Physics and Controlled Fusion* 66 (2024): 035014.

12. R. S. Craxton, K. S. Anderson, T. R. Boehly, et al., "Direct-Drive Inertial Confinement Fusion: A Review," *Physics of Plasmas* 22 (2015): 110501.

13. J. P. Brodrick, R. J. Kingham, M. M. Marinak, et al., "Testing Nonlocal Models of Electron Thermal Conduction for Magnetic and Inertial Confinement Fusion Applications," *Physics of Plasmas* 24 (2017): 092309.

14. A. R. Bell, R. G. Evans, and D. J. Nicholas, "Electron Energy Transport in Steep Temperature Gradients in Laser-Produced Plasmas," *Physical Review Letters* 46 (1981): 243–246.

15. J. F. Luciani, P. Mora, and J. Virmont, "Nonlocal Heat Transport due to Steep Temperature Gradients," *Physical Review Letters* 51 (1983): 1664–1667.

16. A. Thomas, M. Tzoufras, A. Robinson, et al., "A Review of Vlasov–Fokker–Planck Numerical Modeling of Inertial Confinement Fusion Plasma," *Journal of Computational Physics* 231 (2012): 1051.

17. H. P. Le, M. Sherlock, and H. A. Scott, "Influence of Atomic Kinetics on Inverse Bremsstrahlung Heating and Nonlocal Thermal Transport," *Physical Review E* 100 (2019): 013202.

18. G. P. Schurtz, P. D. Nicolaï, and M. Busquet, "A Nonlocal Electron Conduction Model for Multidimensional Radiation Hydrodynamics Codes," *Physics of Plasmas* 7 (2000): 4238–4249.

19. W. Manheimer, D. Colombant, and V. Goncharov, "The Development of a Krook Model for Nonlocal Transport in Laser Produced Plasmas. I. Basic Theory," *Physics of Plasmas* 15 (2008): 083103.

20. A. Marocchino, M. Tzoufras, S. Atzeni, et al., "Comparison for Non-Local Hydrodynamic Thermal Conduction Models," *Physics of Plasmas* 20 (2013): 022702.

21. M. Sherlock, J. P. Brodrick, and C. P. Ridgers, "A Comparison of Non-Local Electron Transport Models for Laser-Plasmas Relevant to Inertial Confinement Fusion," *Physics of Plasmas* 24 (2017): 082706.

22. K. H. Ma, M. V. Patel, M. Sherlock, W. A. Farmer, and E. Johnsen, "Thermal Transport Modeling of Laser-Irradiated Spheres," *Physics of Plasmas* 29 (2022): 112307.

23. W. A. Farmer, C. Bruulsema, G. F. Swadling, et al., "Validation of Heat Transport Modeling Using Directly Driven Beryllium Spheres," *Physics of Plasmas* 27 (2020): 082701.

24. W. A. Farmer, M. D. Rosen, G. F. Swadling, et al., "Investigation of Heat Transport Using Directly Driven Gold Spheres," *Physics of Plasmas* 28 (2021): 032707.

25. R. C. Malone, R. L. McCrory, and R. L. Morse, "Indications of Strongly Flux-Limited Electron Thermal Conduction in Laser-Target Experiments," *Physical Review Letters* 34 (1975): 721–724.

26. T. D. Arber, T. Goffrey, and C. Ridgers, "Models of Thermal Conduction and Non-Local Transport of Relevance to Space Physics With Insights From Laser–Plasma Theory," *Frontiers in Astronomy and Space Sciences* 10 (2023), https://doi.org/10.3389/fspas.2023.1155124.

27. W. L. Kruer, *The Physics of Laser Plasma Interactions* (CRC Press, 2003).

28. M. Rosen, H. Scott, D. Hinkel, et al., "The Role of a Detailed Configuration Accounting (DCA) Atomic Physics Package in Explaining the Energy Balance in Ignition-Scale Hohlraums," *High Energy Density Physics* 7 (2011): 180.

29. V. N. Goncharov, O. V. Gotchev, E. Vianello, et al., "Early Stage of Implosion in Inertial Confinement Fusion: Shock Timing and Perturbation Evolution," *Physics of Plasmas* 13 (2006): 012702.

30. J. Li, B. Zhao, H. Li, and J. Zheng, "Study of Flux Limiter Using Fokker–Planck and Fluid Simulations of Planar Laser-Driven Ablation," *Plasma Physics and Controlled Fusion* 52 (2010): 085008.

31. C. Sijoy, S. Chaurasia, V. Mishra, et al., "An Improved Time-Dependent Nonlocal Electron Heat-Flux Model and Its Verification by Laser-Driven Al Foil Acceleration Experiment," *High Energy Density Physics* 11 (2014): 36.

32. I. Fomenkov, D. Brandt, A. Ershov, et al., "Light Sources for High-Volume Manufacturing EUV Lithography: Technology, Performance, and Power Scaling," *Advanced Optical Technologies* 6 (2017): 173.

33. V. Bakshi, ed., *EUV Lithography*, 2nd ed. (SPIE Press, 2018).

34. O. O. Versolato, "Physics of Laser-Driven Tin Plasma Sources of EUV Radiation for Nanolithography," *Plasma Sources Science and Technology* 28 (2019): 083001.

35. G. O'Sullivan, B. Li, R. D'Arcy, et al., "Spectroscopy of Highly Charged Ions and Its Relevance to EUV and Soft X-Ray Source Development," *Journal of Physics B: Atomic, Molecular and Optical Physics* 48 (2015): 144025.

36. S. Bajt, J. B. Alameda, T. W. Barbee, Jr., et al., "Improved Reflectance and Stability of Mo-Si Multilayers," *Optical Engineering* 41 (2002): 1797.

37. F. Torretti, J. Sheil, R. Schupp, et al., "Prominent Radiative Contributions From Multiply-Excited States in Laser-Produced Tin Plasma for Nanolithography," *Nature Communications* 11 (2020): 2334.

38. J. Sheil, O. O. Versolato, A. J. Neukirch, and J. Colgan, "Multiply-Excited States and Their Contribution to Opacity in CO_2 Laser-Driven Tin-Plasma Conditions," *Journal of Physics B: Atomic, Molecular and Optical Physics* 54 (2021): 035002.

39. A. Sasaki, "Effect of Multiply Excited States to the EUV Emission From Yttrium-Like Tin," *Applied Physics Letters* 124 (2024): 064104.

40. G. Yan, C. Gao, Y. Hou, et al., "Theoretical Investigations on the Radiative Opacity of Sn Plasmas With an Open 4d Orbital Using a Detailed-Level Accounting Model," *Physics of Plasmas* 31 (2024): 093303.

41. M. M. Basko, "On the Maximum Conversion Efficiency Into the 13.5-nm Extreme Ultraviolet Emission Under a Steady-State Laser Ablation of Tin Microspheres," *Physics of Plasmas* 23 (2016): 083114.

42. J. Sheil, O. O. Versolato, V. Bakshi, and H. A. Scott, "Review of the 1st EUV Light Sources Code Comparison Workshop," *Atoms* 11 (2023): 130.

43. I. Tamer, B. A. Reagan, T. Galvin, et al., "1 GW Peak Power and 100 J Pulsed Operation of a Diode-Pumped Tm:YLF Laser," *Optics Express* 30 (2022): 46336.

44. L. Behnke, R. Schupp, Z. Bouza, et al., "Extreme Ultraviolet Light From a Tin Plasma Driven by a 2-μm-Wavelength Laser," *Optics Express* 29 (2021): 4475.

45. Y. Mostafa, L. Behnke, D. J. Engels, et al., "Production of 13.5 nm Light With 5% Conversion Efficiency From 2μm Laser-Driven Tin Microdroplet Plasma," *Applied Physics Letters* 123 (2023): 234101.

46. S. J. J. de Lange, D. J. Hemminga, Y. Mostafa, R. A. Meijer, O. O. Versolato, and J. Sheil, "Modeling the Hundreds-of-Nanoseconds-Long Irradiation of Tin Droplets With a 2μm-Wavelength Laser for Future EUV Lithography," *Plasma Sources Science and Technology* 33 (2024): 105003.

47. Y. Mostafa, L. Behnke, D. J. Engels, and O. O. Versolato, "Mass Use in 2 μm Laser-Driven Tin Plasma Using Sheet Targets," *Journal of Applied Physics* 138 (2025): 143304.

48. T. Sizyuk and A. Hassanein, “Tuning Laser Wavelength and Pulse Duration to Improve the Conversion Efficiency and Performance of EUV Sources for Nanolithography,” *Physics of Plasmas* 27 (2020): 103507.

49. Y. Yuan, Y. Y. Ma, W. P. Wang, et al., “Enhancing the Conversion Efficiency of Extreme Ultraviolet Light Sources Using a 2 μm Wavelength Laser,” *Plasma Physics and Controlled Fusion* 64 (2021): 025001.

50. Z. Y. Shi, Y. Yuan, W. P. Wang, et al., “Enhanced Extreme Ultraviolet Conversion Efficiency of a 2μm Laser-Driven Preformed Tin-Droplet Target Using Short Picosecond Pre-Pulses,” *Physics of Plasmas* 30 (2023): 043107.

51. A. Sunahara, K. Nishihara, and A. Sasaki, “Optimization of Extreme Ultraviolet Emission From Laser-Produced Tin Plasmas Based on Radiation Hydrodynamics Simulations,” *Plasma and Fusion Research* 3 (2009): 043, https://doi.org/10.1585/pfr.3.043.

52. A. Sunahara, A. Hassanein, K. Tomita, S. Namba, and T. Higashiguchi, “Optimization of Extreme Ultra-Violet Light Emitted From the CO_2 Laser-Irradiated Tin Plasmas Using 2D Radiation Hydrodynamic Simulations,” *Optics Express* 31 (2023): 31780–31795.

53. D. J. Hemminga, O. O. Versolato, and J. Sheil, “Simulations of Plasmas Driven by Laser Wavelengths in the 1.064–10.6 μm Range for Their Characterization as Future Extreme Ultraviolet Light Sources,” *Physics of Plasmas* 30 (2023): 033301.

54. J. Gonzalez and J. Sheil, “On the Role of Target Mass in Extreme Ultraviolet Light Generation From CO_2-Driven Tin Plasmas for Nanolithography,” *Physics of Plasmas* 31 (2024): 050701.

55. Q. Min, Z. Xu, S. He, et al., “RHDLPP: A Multigroup Radiation Hydrodynamics Code for Laser-Produced Plasmas,” *Computer Physics Communications* 302 (2024): 109242.

56. V. Sizyuk, A. Hassanein, and T. Sizyuk, “Three-Dimensional Simulation of Laser-Produced Plasma for Extreme Ultraviolet Lithography Applications,” *Journal of Applied Physics* 100 (2006): 103106.

57. Y. L. Dong, B. H. Xu, X. H. Yang, et al., “Enhanced Extreme Ultraviolet Emission From a Transverse Profile-Tailored Laser-Driven Preformed Tin Disk Targets,” *Optics Express* 33 (2025): 43894–43906.

58. A. B. Langdon, “Nonlinear Inverse Bremsstrahlung and Heated-Electron Distributions,” *Physical Review Letters* 44 (1980): 575–579.

59. J. Gonzalez and J. Sheil, “Langdon Effect in the Realm of Extreme Ultraviolet Source Plasmas,” *Physical Review E* 111 (2025): L023201.

60. M. Basko, J. Maruhn, and A. Tauschwitz, “GSI Report 1,” 410, 2010.

61. D. Kurilovich, M. M. Basko, D. A. Kim, et al., “Power-Law Scaling of Plasma Pressure on Laser-Ablated Tin Microdroplets,” *Physics of Plasmas* 25 (2018): 012709.

62. J. Hernandez-Rueda, B. Liu, D. J. Hemminga, et al., “Early-Time Hydrodynamic Response of a Tin Droplet Driven by Laser-Produced Plasma,” *Physical Review Research* 4 (2022): 013142.

63. D. J. Hemminga, L. Poirier, M. M. Basko, et al., “High-Energy Ions From Nd:YAG Laser Ablation of Tin Microdroplets: Comparison Between Experiment and a Single-Fluid Hydrodynamic Model,” *Plasma Sources Science and Technology* 30 (2021): 105006.

64. L. Poirier, D. J. Hemminga, A. Lassise, et al., “Strongly Anisotropic Ion Emission in the Expansion of Nd:YAG-Laser-Produced Plasma,” *Physics of Plasmas* 29 (2022): 123102.

65. M. M. Basko, V. G. Novikov, and A. S. Grushin, “On the Structure of Quasi-Stationary Laser Ablation Fronts in Strongly Radiating Plasmas,” *Physics of Plasmas* 22 (2015): 053111.

66. H. Brysk, P. M. Campbell, and P. Hammerling, “Thermal Conduction in Laser Fusion,” *Plasma Physics* 17 (1975): 473–484.

67. M. Basko, J. Maruhn, and A. Tauschwitz, “RALEF-2D: A 2D Hydrodynamic Code With Heat Conduction and Radiation Transport,” Tech. Rep., 2017.

68. M. Lampe, “Transport Coefficients of Degenerate Plasma,” *Physics Review* 170 (1968): 306–319.

69. M. Basko, T. Löwer, V. N. Kondrashov, A. Kendl, R. Sigel, and J. Meyer-ter Vehn, “Optical Probing of Laser-Induced Indirectly Driven Shock Waves in Aluminum,” *Physical Review E* 56 (1997): 1019.

70. D. G. Colombant, W. M. Manheimer, and M. Busquet, “Test of Models for Electron Transport in Laser Produced Plasmas,” *Physics of Plasmas* 12 (2005): 072702.

71. J. Sheil, L. Poirier, A. C. Lassise, et al., “Power-Law Scaling Relating the Average Charge State and Kinetic Energy in Expanding Laser-Driven Plasmas,” *Physical Review Letters* 133 (2024): 125101.

72. K. Tomita, Y. Sato, S. Tsukiyama, et al., “Time-Resolved Two-Dimensional Profiles of Electron Density and Temperature of Laser-Produced Tin Plasmas for Extreme-Ultraviolet Lithography Light Sources,” *Scientific Reports* 7 (2017): 12328.

73. K. Tomita, Y. Pan, A. Sunahara, K. Kouge, H. Mizoguchi, and K. Nishihara, “Observation of Plasma Inflows in Laser-Produced Sn Plasma and Their Contribution to Extreme-Ultraviolet Light Output Enhancement,” *Scientific Reports* 13 (2023): 1825.

74. Y. Pan, K. Tomita, A. Sunahara, A. Sasaki, and K. Nishihara, “Joint Measurement of Electron Density, Temperature, and Emission Spectrum of Nd:YAG Laser-Produced Tin Plasma,” *Applied Physics Letters* 123 (2023): 204103.

75. J. P. Matte, M. Lamoureux, C. Moller, et al., “Non-Maxwellian Electron Distributions and Continuum X-Ray Emission in Inverse Bremsstrahlung Heated Plasmas,” *Plasma Physics and Controlled Fusion* 30 (1988): 1665–1689.

76. P. Mora and H. Yahi, “Thermal Heat-Flux Reduction in Laser-Produced Plasmas,” *Physical Review A* 26 (1982): 2259–2261.

77. K. Li and W. Y. Huo, “Nonlocal Electron Heat Transport Under the Non-Maxwellian Distribution Function,” *Physics of Plasmas* 27 (2020): 062705.

78. N. R. Shaffer, A. V. Maximov, and V. N. Goncharov, “Thermal Conductivity of a Laser Plasma,” *Physical Review E* 108 (2023): 045205.

79. W. Yi Huo, K. Lan, P. Jun Gu, H. Yong, and Q. Hong Zeng, “Electron Heat Conduction Under Non-Maxwellian Distribution in Hohlraum Simulation,” *Physics of Plasmas* 19 (2012): 012313.